scientific reports

Check for updates

OPEN

RSM approach for process optimization of the photodegradation of congo red by a novel $NiCo_2S_4$/chitosan photocatalyst

Vishal Gadore, Ashish Kumar Singh, Soumya Ranjan Mishra & Md. Ahmaruzzaman✉

The current study reported a facile co-precipitation technique for synthesizing novel $NiCo_2S_4$/chitosan nanocomposite. The photocatalytic activity of the prepared nanocomposite was evaluated using congo red (CR) dye as a target pollutant. The central composite design was employed to examine the impact of different reaction conditions on CR dye degradation. This study selected the pH, photocatalyst loading, initial CR concentration and reaction time as reaction parameters, while the degradation efficiency (%) was selected as the response. A desirability factor of 1 suggested the adequacy of the model. Maximum degradation of 93.46% of 35 ppm dye solution was observed after 60 min of visible light irradiation. The response to surface methodology (RSM) is a helpful technique to predict the optimum reaction conditions of the photodegradation of CR dye. Moreover, $NiCo_2S_4$/Ch displayed high recyclability and reusability up to four consecutive cycles. The present study suggests that the prepared $NiCo_2S_4$/chitosan nanocomposite could prove to be a viable photocatalyst for the treatment of dye-contaminated wastewater.

Secure and pure water availability has become a serious concern because of the persistent and unacceptable discharge of organic contaminants into waterways from various sources[1,2]. These contaminants are regarded as highly toxic and persistent in the ecology, having an impact on both human health and the environment[3,4]. Numerous sectors, including textile, pharmaceutical, nourishment, beauty aids, plastic, rubber, and paper, use significant quantities of organic dyes to colour their goods[5,6]. When released into the ecosystem, these coloured compounds can harm aquatic life and human health and can be observed even at minimal concentrations[7,8]. Organic dyes such as Congo red (CR) have been recognized as potent human carcinogens by the IARC "International Agency for Research on Cancer" due to their ability to induce tumours in animals[9]. It contaminates water and soil, leading to harmful effects on aquatic organisms and other wildlife.

Many traditional techniques for cleaning wastewater, including biodegradation, electrochemical combustion, and chemical oxidation, are ineffective in removing organic pollutants[9,10]. A heterogeneous photocatalysis method using semiconductor heterojunctions as photocatalysts has been designed to efficiently utilize solar power as a visible source to degrade organic pollutants from water[11]. Recent research has demonstrated that photocatalysis methods are thought to be the most effective and practical methods for eliminating organic matter from wastewater due to their high rate of degradation, reduced generation of secondary pollutants, efficacy, and cost-effectiveness[12,13]. Photocatalysis is the term for the light-induced chemical reaction that generates electron and hole pairs when subjected to sufficiently strong light. Reactive oxygen species (ROS), such as superoxide ($^{\bullet}O_2$) and hydroxyl ($^{\bullet}OH$) radicals, are generated when these photogenerated electron/hole pairs interact with oxygen and water. These ROS then attack the target pollutants, degrading them into less harmful intermediates and ultimately converting them into carbon dioxide and water[14,15].

Metal sulfides have recently attracted much interest as possible heterogeneous catalysts for the photodegradation organic molecules. They have become an excellent replacement for conventional catalysts due to their increased surface area, porous structure, better charge transportation property, non-toxicity, and appropriate bandgap energy suitable for visible regions[16]. However, research into their extensive uses for removing

Department of Chemistry, National Institute of Technology Silchar, Silchar, Assam 788010, India. ✉email: mda2002@gmail.com

contaminants from industrial effluent is still lacking. In addition, many currently available sulfide-based photocatalysts such as ZnS/ZnO[17], CuS/CdS[18], MoS_2[19], etc., have poor effectiveness restrictions and are only helpful in situations where the amount of pollutants is very low. Due to their superior electrical and redox responses, mixed metal sulphides (MMSs) significantly outperform mono-metal sulphides in photocatalytic performance[20]. Nickel–cobalt sulfide ($NiCo_2S_4$), a significant ternary transition metal sulfide, has recently received great attention as a potential photocatalyst owing to its optimum bandgap, chemical and thermal resistivity, and quantum size impact[21]. $NiCo_2S_4$ has emerged as an effective photocatalyst for water treatment due to its narrow bandgap energy of 1.2–2.4 eV and excellent light harvesting properties[22,23].

Furthermore, recent research using its high carrier density as a basis demonstrated that $NiCo_2S_4$ is undoubtedly a metal and not a semiconductor substance[24]. However, $NiCo_2S_4$ suffers from a limitation of firstly, faster charge recombination rate and, secondly, agglomeration of nanoparticles during synthesis[25]. Therefore, $NiCo_2S_4$ utilization as a useful catalyst material for visible-light-induced photocatalytic degradation is still challenging. Thus, the effectiveness of $NiCo_2S_4$ for the photodegradation of organic pollutants could be enhanced by forming a nanocomposite, which will prevent its agglomeration and slow down the charge recombination rate[26].

Biopolymer-doped metal hydroxides, oxides, and sulfides proved to be potential photocatalysts for degrading dyes from water samples. The efficacy of photodegradation is significantly influenced by biopolymers[27,28]. One of the most prevalent polysaccharides, chitosan (CS) [poly-(1 4) 2-amino-2-deoxy-d-glucose], is a cationic biopolymer that is an unprocessed carbohydrate derived from plants and animals. Strong intra- and intermolecular hydrogen interactions are present in this semi-crystalline polymer. In addition to being steady and secure, it is also reactive, biocompatible, and compostable. It is possible to modify chitosan because it contains volatile amino- and hydroxyl groups[29]. Chitosan is widely used in numerous biological and chemical applications because of its biological traits, non-toxicity, ability to fight cancer, antioxidant properties, ability to heal wounds[30], and its use in water purification[31].

The present study illustrates the synthesis of novel $NiCo_2S_4$/chitosan ($NiCo_2S_4$/Ch) via a simple co-precipitation technique and its applicability as a photocatalyst for degrading CR from an aqueous stream. To our understanding, it's the first research on the degradation of CR using a $NiCo_2S_4$/chitosan nanocomposite. The prepared photocatalyst showed enhanced photodegradation of CR under visible light. The enhanced degradation efficiency was attributed to incorporating chitosan, as it helps delocalize photoinduced charges. The presence of reactive groups (NH_2 and OH) on the chitosan surface could be effective in dye molecule adsorption, which enhances dye degradation by $NiCo_2S_4$ nanoparticles[32]. The effect of reaction parameters on the degradation of CR dye was accessed using response to surface methodology (RSM) with a central composite design (CCD).

Experimentation

Reagents

Chitosan [$C_{18}H_{35}N_3O_{13}$], Nickel (II) nitrate hexahydrate [$Ni(NO_3)_2.6H_2O$], Cobalt (II) nitrate hexahydrate [$Co(NO_3)_2.6H_2O$], Sodium sulfide hydrate [$Na_2S.9H_2O$], Acetic acid [CH_3COOH], Congo red (CR), and distilled water.

The reagents were acquired from Sigma Aldrich and were of excellent analytical quality and used without extra purification. Distilled water was utilized during the experiment.

Synthesis of $NiCo_2S_4$/Ch nanocomposite

The $NiCo_2S_4$/chitosan was synthesized via a facile precipitation technique. Initially, 100 mg of chitosan and 5 mL acetic acid were mixed in a 200 mL beaker under constant stirring until a clear solution was obtained. Then, 30 mL of distilled water was added to the above solution and stirred for 15 min at 50 °C. Meanwhile, 2 mmol of [$Ni(NO_3)_2.6H_2O$] and 4 mmol of [$Co(NO_3)_2.6H_2O$] were dissolved in 50 mL of distilled water under constant stirring for 15 min. The salt solution was then added dropwise to the beaker containing chitosan, and the resultant mixture was stirred for 30 min at 50 °C. In another beaker, a solution of 8 mmol of [$Na_2S.9H_2O$] in 20 mL distilled water was made and added dropwise to the salt solution. A black-coloured precipitate was observed. The resultant mixture was stirred for another 2 h at the same temperature, and the solution was kept for ageing for 24 h. The final black precipitate was centrifuged, washed and kept for drying in an oven at 80 °C for 7 h. The exact process was carried out without chitosan to synthesize pure $NiCo_2S_4$ nanoparticles.

Characterization

The X-ray diffraction (XRD) spectrum of the samples was taken from an X'PERT powder X-ray diffractometer with Cu k_α radiation. The X-ray photoelectron spectrum of $NiCo_2S_4$/chitosan was recorded using a Thermo Fisher Scientific Pvt. Ltd. ESCALAB Xi + X-ray photoelectron spectrometer (XPS). The shape and particle size of the sample were analyzed through a JEOL JEM-2100 PlusElectron high-resolution transmission electron microscope (HRTEM). The morphology and the energy dispersive X-ray analysis (EDAX) of $NiCo_2S_4$/Ch were accessed using a Carl ZEISS SIGMA field emission scanning electron microscope (FESEM). The liquid chromatography-mass spectroscopy (LCMS) spectrum was recorded using a Xevo XS QTof mass spectrometer. Cary 5000 UV–Vis-NIR spectrophotometer was used to record the UV-DRS spectra. The Fourier Transform Infrared (FTIR) spectrum of $NiCo_2S_4$/Ch was recorded using the Perkin Elmer spectrum 100 instrument.

Photodegradation tests

All the photodegradation tests were carried out at room temperature (33 ± 2 °C) in a wooden cabinet equipped with a Philips 23 W white LED bulb as the source of visible light with a light intensity of 52.13 W/m^2. The photodegradation reactions were conducted in a 100 mL beaker with 50 mL dye solution placed 10 cm from the LED light. The light intensity was measured using a Lux meter placed at the base of the beaker.

Typically, in an experiment, the beaker containing 50 mL 35 ppm of dye solution and 22 mg of $NiCo_2S_4$/Ch was irradiated under LED light by placing it in a wooden chamber. The reaction cell was kept in the dark at a constant stirring speed for 30 min to attain adsorption–desorption equilibrium before irradiating it for a prescribed time duration. The dye degradation was examined by tracking the decrease in the absorbance of CR dye at $\lambda_{max} = 497$ nm using a UV–visible spectrophotometer (GENESYS 10 S UV–Visible spectrophotometer).

The photodegradation efficiency was calculated from the following equation[33]:

$$Degradation\ efficiency(\%) = \left(\frac{C_0 - C}{C_0}\right) \times 100 \tag{1}$$

The kinetics of the photodegradation of CR under optimum conditions was evaluated according to the following equation:

$$ln\frac{C_0}{C} = kt \tag{2}$$

C_0 and C are the initial and final concentrations at time t of CR dye, respectively, and k is the pseudo-first-order rate constant.

Experimental design

The effect of the reaction factors such as pH (A), photocatalyst dosage (B), initial dye concentration (C) and time (D) on the photocatalytic activity of $NiCo_2S_4$/Ch catalyst was examined using response to surface methodology (RSM) employing central composite design (CCD). As CR dye is an indicator and is blue in an acidic medium, the study of pH is limited to alkaline conditions. Design Expert Software (DOE) version 13 was used to create the design of the experimental analysis. The RSM is a collection of mathematical and statistical methods that help investigate the effect of individual parameters on the response[34]. These experimental data were fitted to achieve the best degradation efficiency. RSM gives a set of reaction conditions which help examine the effect of single-parameter and multi-parameter interactions and the relationship between operating parameters on the photodegradation rate of CR dye to achieve the optimum conditions[35]. According to the RSM analysis, an experimental design of 30 runs (16-factor points + 8 axial points + 6 replicates) was considered as the empirical model according to the following equation:

$$N = 2^k + 2k + 6 \tag{3}$$

N, Number of experimental runs; and k, Number of input variables (parameters).

A quadratic equation predicted the relation between CR photodegradation and the individual factors. The response was predicted using the following equation[36]:

$$Y = \beta_0 + \sum_{i=1}^{k} \beta_i X_i + \sum_{j=1}^{k} \beta_{jj} X_j^2 + \sum_{i=1}^{k} \sum_{j=1}^{k} \beta_{ij} X_i X_j \tag{4}$$

where X_i is the coded value of the ith individual parameter, β_0, β_i, and β_{ij} are the equation's zero, first and second-order coefficients, respectively.

The analysis of variance (ANOVA) and F-test were used to appraise the results, and the coefficients of R^2 and R^2_{adj} were used to assess the polynomial model's fitness. A careful comparison between the experimental and predicted outcomes was examined at the conclusion to demonstrate the predicted model's statistical significance.

Results and discussion

XRD analysis

The XRD is a useful technique to access the crystal structure of the nanocomposites. The XRD spectra of $NiCo_2S_4$ and $NiCo_2S_4$/Ch are shown in Fig. 1. The XRD spectrum of $NiCo_2S_4$ showed the broad and major diffraction peaks at $2\theta = 31.47°$, 38.19° and 55.10° could be assigned to (311), (500), and (440) planes of cubic $NiCo_2S_4$, respectively, matching with the JCPDS card No. 43-1477, having lattice parameter $a = b = c = 9.417$ Å[37]. The broad peaks in the XRD spectrum indicate the amorphous nature of the sample[38]. The XRD spectrum of $NiCo_2S_4$/Ch showed a shift of the peaks to a higher angle because of the distortion in the growth phase of $NiCo_2S_4$ due to the presence of chitosan[39], and all the peaks corresponding to (311), (500), and (440) planes of cubic $NiCo_2S_4$ could be identified. The sift of the peaks and the appearance of a new peak at $2\theta = 20.0°$ appeared, indicating the incorporation of chitosan in the nanocomposite[40]. The average crystallite size of the $NiCo_2S_4$/Ch nanocomposite was found to be 8.17 nm using Debye–Scherrer's equation.

Morphological and elemental analysis

The SEM images of the $NiCo_2S_4$/Ch nanocomposite illustrated in Fig. 2a–c displayed that the surface of the prepared sample was rough due to the dispersion of small spherical $NiCo_2S_4$ nanoparticles over the chitosan surface. The presence of small granular $NiCo_2S_4$ nanoparticles could be seen in the high-resolution SEM images. The TEM images of $NiCo_2S_4$/Ch nanocomposite showed an irregular distribution of $NiCo_2S_4$ nanoparticles over the chitosan (Fig. 2d). Clear lattice planes with lattice fringes of spacing 0.3 nm corresponding to (400) lattice plane of $NiCo_2S_4$ could be identified and marked in the HRTEM images of $NiCo_2S_4$/Ch nanocomposite (Fig. 2e,f). The size distribution histogram was plotted, and the average particle size could be calculated from the histogram seen in Fig. 2h. An average particle of the $NiCo_2S_4$/Ch nanocomposite was observed to be 10.0 nm in accordance with

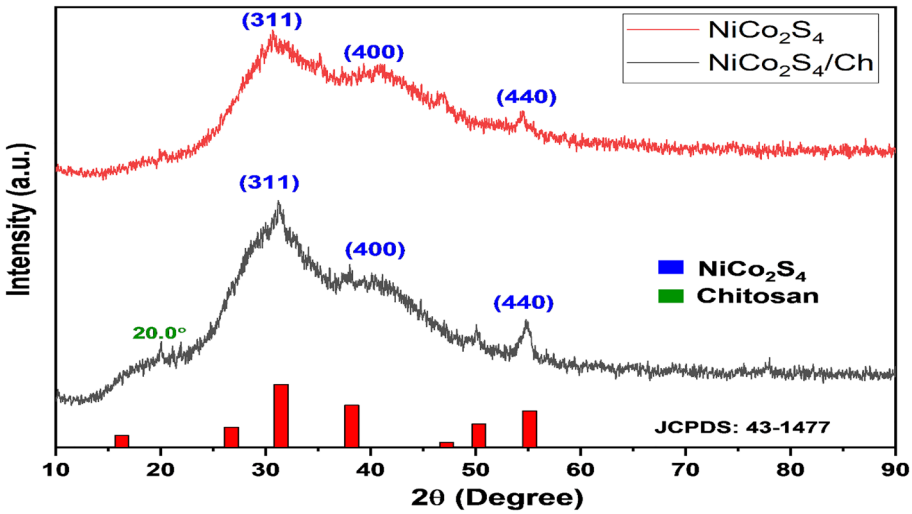

Figure 1. XRD spectrum of $NiCo_2S_4$ and $NiCo_2S_4$/Ch.

the average crystallite size. The EDAX spectrum (Fig. 2g) revealed the presence of nickel, cobalt, sulfur, oxygen and carbon with relative atomic percentages of 5.72%, 12.47%, 22.25%, 31.73%, and 27.83%. At the same time, a higher amount of carbon and oxygen is due to the chitosan[41].

XPS analysis

The oxidation states and elemental composition of the $NiCo_2S_4$/Ch nanocomposite were analyzed through XPS. The survey spectrum of $NiCo_2S_4$/Ch showed the presence of Ni 2p, Co 2p, S 2p, C 1s, O 1s and N 1s as expected (Fig. 3a). As seen in Fig. 3b, the short scan of C 1s showed a triplet of peaks appearing at 284.4 eV, 258.8 eV and 288.2 eV. The peaks at lower binding energies, i.e. 284.4 eV and 258.8 eV, are attributed to the carbon as in C–C/C–H and C–O/C–N bonds, respectively[42]. The higher binding energy peak at 288.2 eV shows the presence of sp^2 hybridized carbon in C=O or C–O–C bonds[43]. The short scan spectrum of O 1s (Fig. 3c) showed a doublet of peaks appearing at 531.3 eV assigned to C=O and 532.2 eV due to C–O–C bonds[44]. A shift in the binding energies to greater values for C 1s and O 1s in $NiCo_2S_4$/Ch could be attributed to the insertion of $NiCo_2S_4$ nanoparticles, which increased the electron density near C and O, causing a shift in the binding energies to higher values[45]. The core-level spectrum of N 1s is shown in Fig. 3d. Here, a doublet of peaks was also observed, similar to the O 1s spectrum. The peaks appeared at 399.8 eV and 400.2 eV, which could be assigned to C–NH and C–NH_2 groups, respectively[46]. Figure 3e illustrates the deconvoluted spectrum of Ni 2p, showing the presence of a pair of doublets and satellite (Sat.) peaks. The 856.5 eV and 874.5 eV peaks correspond to Ni $2p_{3/2}$ and Ni $2p_{1/2}$, respectively, characteristic of the + 3 oxidation state of Ni atoms, while the peaks at 853.0 eV and 876.2 eV are distinctive of Ni^{+2} atoms, indicting the co-existence of Ni^{+2} and Ni^{+3} ions in $NiCo_2S_4$/Ch composite[47]. Figure 3f shows the deconvoluted short scan of Co 2p, which is quite similar to Ni 2p spectra. The strong peaks at 782.0 eV could be assigned to Co $2p_{3/2}$, and the peak at 798.1 eV corresponds to Co $2p_{1/2}$, indicating the presence of Co^{+2} ions, while the peaks at 778.0 eV and 793.1 eV are characteristic of Co^{+3} ions which is also present in small amounts, suggesting the co-existence of Co^{+2} and Co^{+3} ions in the composite[48]. The peaks at 784.5 eV and 802.5 eV are the satellite peaks of Co 2p. The typical short scan spectra of S 2p showed two main peaks and a satellite peak (Fig. 3g). The peaks at 161.2 eV and 162.7 eV are the characteristic peaks of S $2p_{3/2}$ and S $2p_{1/2}$, respectively, attributed to the − 2 oxidation state of sulfur[49,50].

Functional group analysis

The presence of the chitosan and the surface functional group were also analyzed using FTIR spectroscopy. The FTIR spectrum of $NiCo_2S_4$ and $NiCo_2S_4$/Ch nanocomposite is illustrated in Fig. 4. Pure $NiCo_2S_4$, being an inorganic compound, showed two peaks at 1110 and 1068 cm^{-1} attributed to C–O stretching in adsorbed carbon dioxide. A wide peak in the region 3500–3000 cm^{-1} occurred due to the stretching of O–H and N–H bonds of chitosan overlapping in the same region. Two small peaks at 2917 cm^{-1} and 2852 cm^{-1} are the characteristic stretching bands of C–H groups present in chitosan[51]. The occurrence of C=O bond stretching is indicated by a broad and strong peak at 1599 cm^{-1}. The peak at 1438 cm^{-1} was ascribed to the bending vibrations of CH_2 groups. A strong band between 1029 and 1002 cm^{-1} corresponds to the stretching of C–O bonds. The bands at 914 cm^{-1} and 719 cm^{-1} indicate the out-of-plane bendings of C–H groups. All these bands in the FTIR spectrum of $NiCo_2S_4$/Ch nanocomposite agree with the previous literature and confirm the existence of chitosan in the prepared material[52]. Meanwhile, a small band at 584 cm^{-1} arises due to metal–oxygen stretchings[53].

Optical properties

The optical and light harvesting behaviour of $NiCo_2S_4$ nanoparticles and $NiCo_2S_4$/Ch nanocomposite were investigated using UV-DRS. The absorption spectra of $NiCo_2S_4$ nanoparticles and $NiCo_2S_4$/Ch nanocomposite are

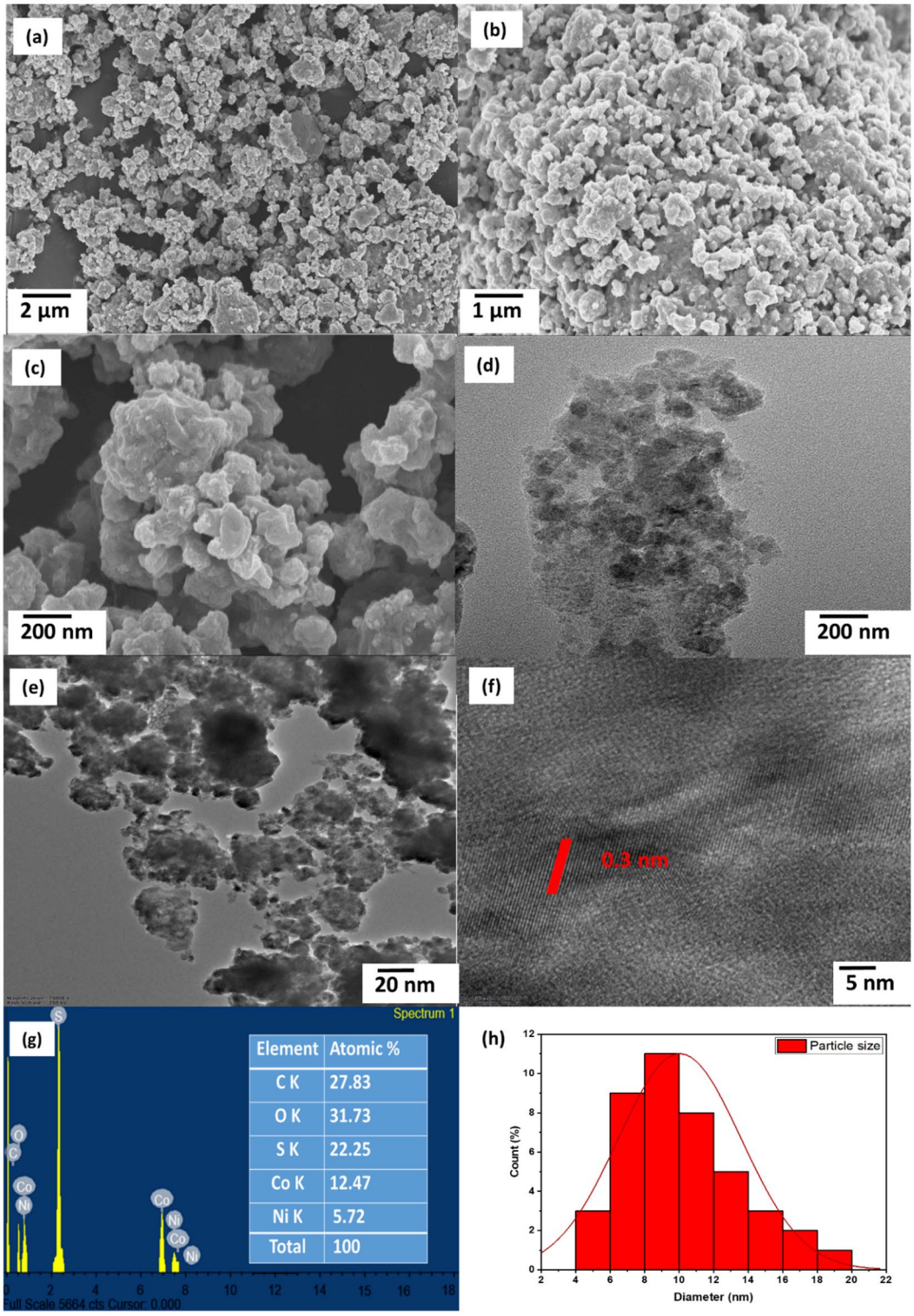

Figure 2. (**a**–**c**) SEM images, (**d**) TEM image, (**e**–**f**) HRTEM images, (**g**) EDAX spectrum and (**h**) size distribution histogram of $NiCo_2S_4$/Ch nanocomposite.

shown in Fig. 5. Both the samples showed maximum absorption in the range of 300–310 nm. However, $NiCo_2S_4$/Ch nanocomposite showed higher absorption intensity compared to pure $NiCo_2S_4$ nanoparticles, indicating improved light harvesting properties. Additionally, both the samples showed strong absorption in the whole UV–visible region, suggesting the excellent light absorption tendency of $NiCo_2S_4$. The band gap of the photocatalyst was calculated using Tauc's plot according to the following equation:

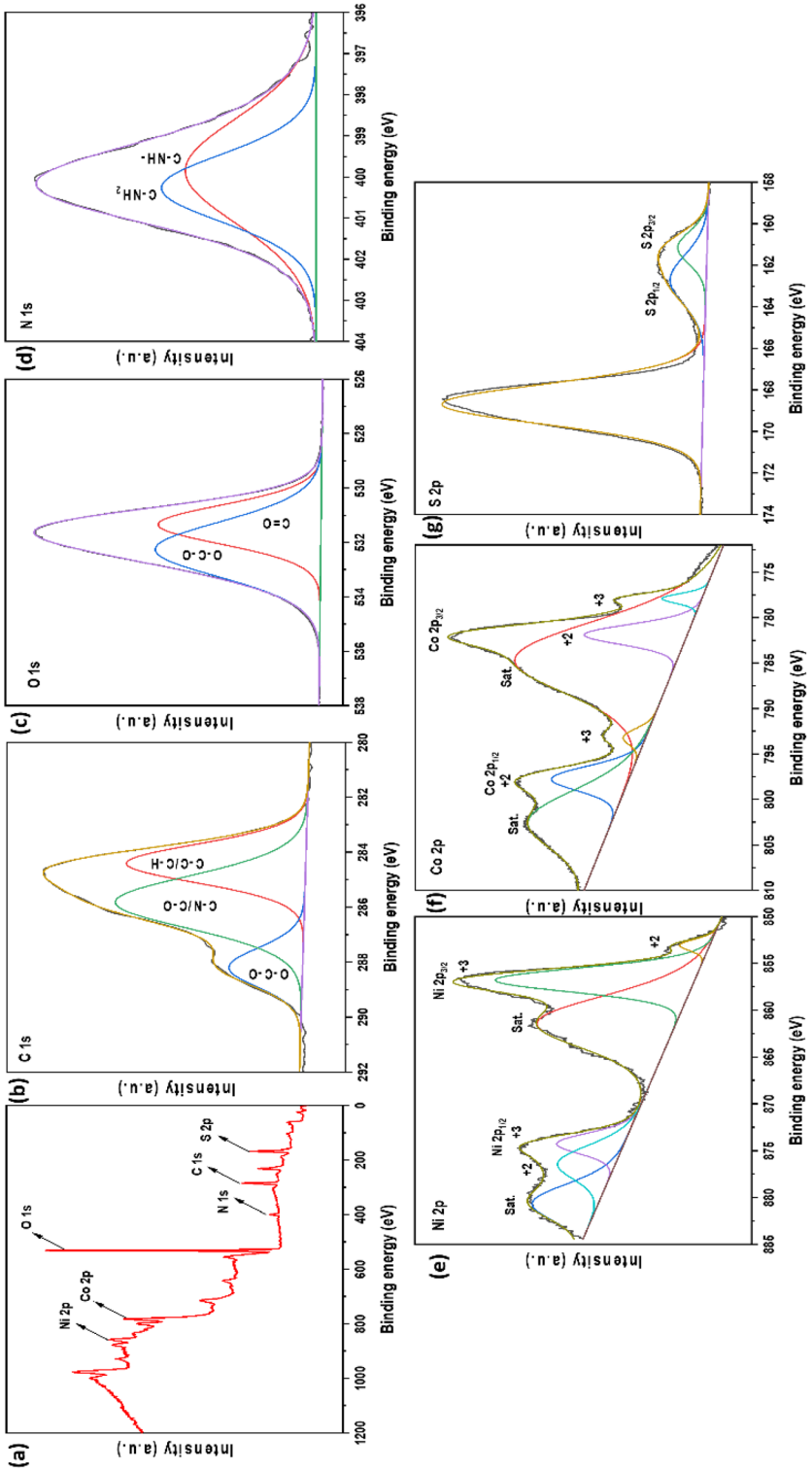

Figure 3. (**a**) XPS survey, short scan of (**b**) C 1s, (**c**) O 1s, (**d**) N 1s, (**e**) Ni 2p, (**f**) Co 2p and (**g**) S 2p.

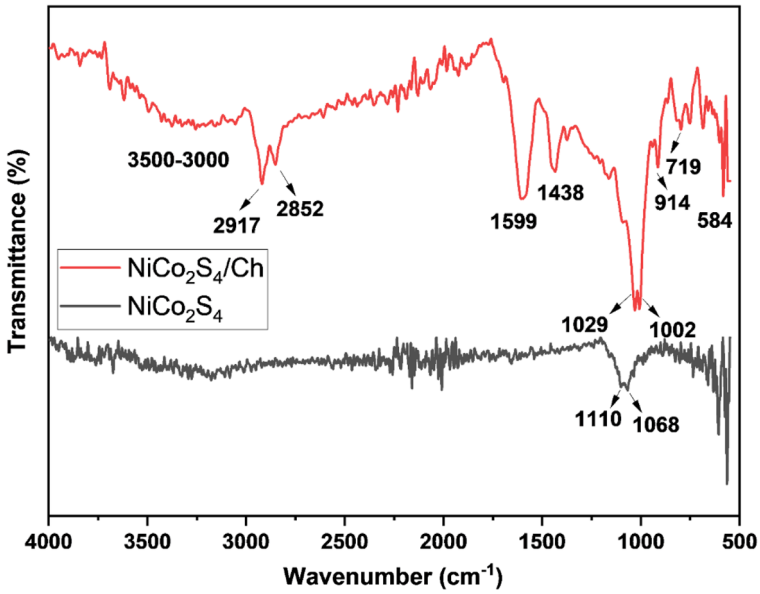

Figure 4. FTIR spectrum of pure $NiCo_2S_4$ and $NiCo_2S_4$/Ch nanocomposite.

$$(\alpha h\nu)^n = A\left(h\nu - E_g\right) \tag{5}$$

here α, Coefficient of absorption; h, Planck's constant; ν, Frequency of light; A, Constant; E_g, Optical bandgap of the material, and n is ½ for indirect and 2 for direct allowed transitions, respectively.

$NiCo_2S_4$ nanoparticles displayed a bandgap of 2.2 eV, which is in good agreement with the formerly published studies[54]. The bandgap reduced from 2.2 to 2.0 eV for the $NiCo_2S_4$/Ch nanocomposite, possibly due to increased particle size after forming the nanocomposite[55]. Additionally, a low bandgap of the material indicates high light-harvesting abilities.

One useful method for determining the visible light photocatalytic activity of the produced nanocomposites is photoluminescence (PL) spectroscopy. The higher intensity of the PL peak indicates a faster rate of electron–hole recombination and a lower photocatalytic activity, while a low-intensity PL peak has a slower charge recombination rate and a higher photocatalytic activity[56]. In the PL spectrum, pristine $NiCo_2S_4$ displayed the maximum intensity, indicating the highest charge recombination rate (Fig. 5c). When chitosan and $NiCo_2S_4$ are combined, the PL peak's intensity drops. Higher photocatalytic activity requires a substantially lower charge recombination rate, which is indicated by the drop in PL intensity[57]. As expected, the $NiCo_2S_4$/Ch nanocomposite displayed the highest photocatalytic activity and the lowest intensity in the PL spectrum, indicating the slowest charge recombination rate.

Optimization of CR degradation using RSM

RSM was used to examine how response factors affected CR's degradation rate. The experimental design was formulated by CCD to attain maximum degradation efficiency of CR in aqueous solutions by adjusting the reaction parameters. CCD formulated an experimental array of 30 runs, and the predicted and actual responses, along with the four reaction parameters, i.e. pH (A), catalyst dosage (B), initial dye concentration (C) and reaction time (D), are shown in Table 1. The predicted equation of CR degradation was as follows:

$$\begin{aligned}\text{Degradation}(\%) = {} & 93.64 + 0.9175A + 1.51B - 2.17C + 6.69D + 0.3313AB - 0.1700AC \\ & - 0.0787AD - 0.2962BC - 0.5225BD - 0.3762CD - 1.93A^2 - 2.13B^2 - 1.67C^2 - 11.63D^2\end{aligned} \tag{6}$$

The equation above represents the combined effect of several factors on the CR degrading efficiency (%). Contrarily, the response is affected favourably and unfavourably by the coefficients with positive and negative values, respectively.

ANOVA was used extensively to examine the impact of the constructed RSM model on the CR degradation efficiency[58]. The ANOVA results and the summary of the quadratic model are given in Table 2. As seen in Table 2, a low *P*-value (< 0.0001), an F-value of 219.11, and a high sum of square values of 2600.50 indicated that the quadratic model is the most suitable. The results reproducibility and the model's implication are generally assessed based on the coefficient of variance (CV) percentage. A CV % ranging between 0.5 and 13.5% is considered an optimum value. Here, a low CV value of just 1.11% indicated a high reproducibility of the proposed quadratic model. Furthermore, a higher value of correlation coefficients ($R^2 = 0.995$, Adj $R^2 = 0.990$ and Pred $R^2 = 0.961$) indicated a well-fitted model[59]. The adequate precision of 43.12 for the degradation of CR shows a good response. A ratio larger than 4 is preferable, showing that the model's mean can deliver the expected performance[60]. The linear fit of actual vs predicted values for CR degradation ($R^2 = 0.995$) is shown in Fig. 6a.

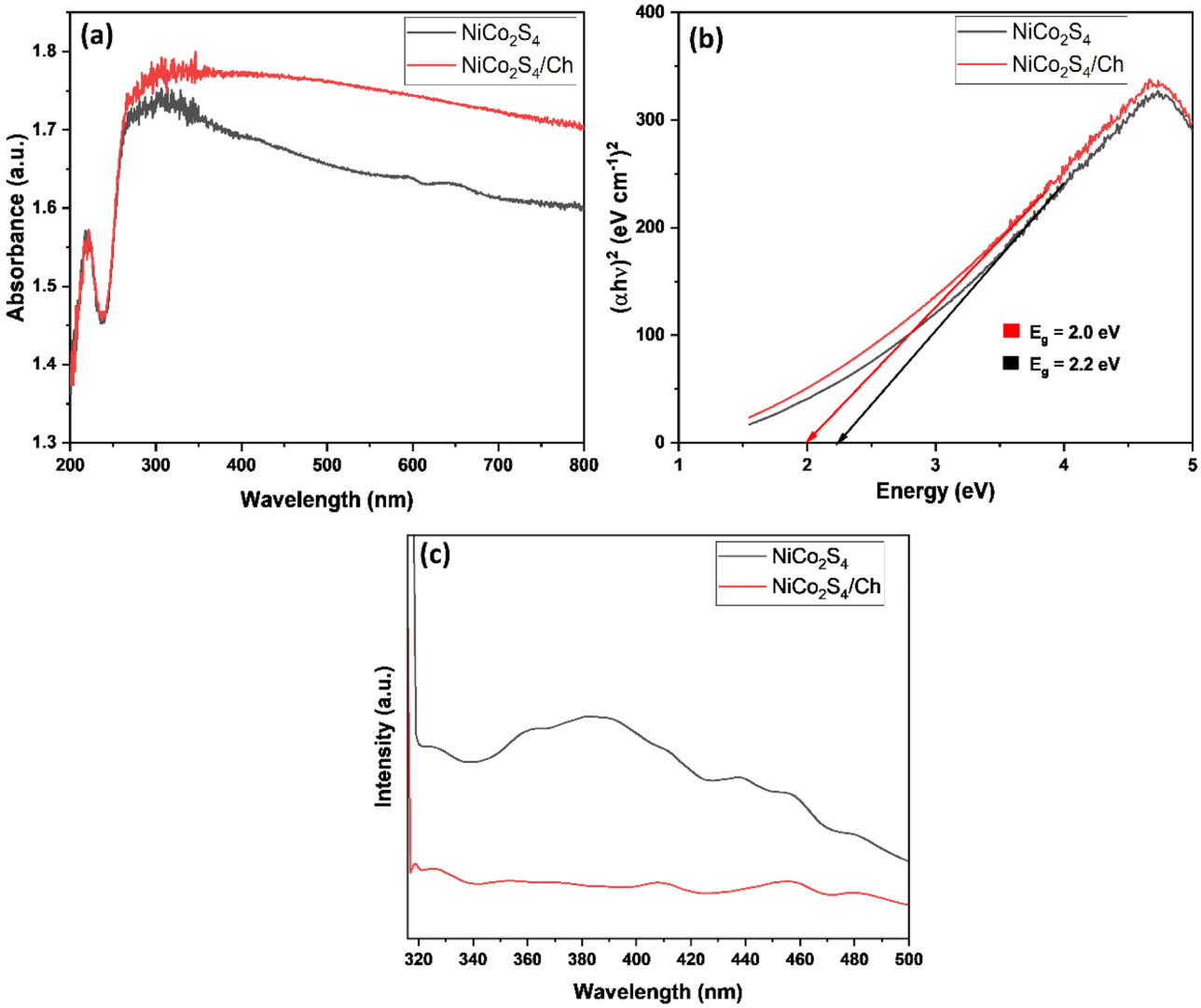

Figure 5. (**a**) The absorption spectrum, (**b**) Tauc's plot, and (**c**) PL spectrum of $NiCo_2S_4$ and $NiCo_2S_4$/Ch.

The plot of residuals vs experimental runs (Fig. 6b,c) depicted all residuals are within ± 4%, indicating the model can predict a good response. The Box-cox plot (Fig. 6d) for power transforms showed a lambda value of 1, demonstrating that the response does not require transformation for the degradation of CR. These results confirm that this model could be used to predict the degradation efficiency of CR dye.

The relation between various independent factors on the degradation of CR was assessed by developing 3D response surfaces. The results of the interactions among the four parameters are shown in Fig. 7. Figure 7a shows the relation between the pH and catalyst dosage. The degradation process is not considerably impacted by pH. However, the degradation efficiency increases with increasing photocatalyst dosage and starts to decline above the optimum value. The upsurge in the photocatalyst dosage instigated a temporary rise in degradation efficiency brought on by the more active sites. However, the decline in the degradation efficiency of the dye was due to the increased opacity of the solution hindering the photons from reaching the catalyst's surface[61]. Figure 7b illustrates the relationship between pH and dye concentration affecting the rate of CR degradation. A low dye concentration causes a higher degradation rate. The plot of pH and time relating to degradation efficiency shows an initial increase in the degradation, which slumps after the optimum time duration (Fig. 7c). Figure 7d shows the relation between catalyst dosage and dye concentration. The degradation increases at decreasing CR concentration and increasing photocatalyst loading. The relation of catalyst dosage and dye concentration with time is illustrated in Fig. 7e,f. The photodegradation efficiency increases with increasing catalyst dosage and decreasing dye concentration. Similar trends were also observed in various studies investigating the photodegradation of dyes[62,63]. Optimization of these parameters is essential to maximize degradation efficiency and reduce the time and cost of operation. Therefore, in order to get the highest CR dye degradation efficiency, all four parameters were optimized.

The RSM has predicted the optimum pH to be 9, catalyst dosage of 21.5 mg, CR concentration of 35 ppm and radiation time of 67 min to attain a maximum degradation efficacy of 93.51% with a desirability value of 1.00. The $NiCo_2S_4$/Ch nanocomposite was shown to be a potential photocatalytic material for the degradation of

Runs	pH	Catalyst dosage (mg)	Dye concentration (ppm)	Time (min)	Degradation efficiency (%)		Residual
					Experimental	Predicted	
1	8	24	40	45	66.76	68.19	−1.43
2	9	22	35	60	93.46	93.46	0
3	8	20	30	75	82.55	83.37	−0.8183
4	9	18	35	60	82.31	81.92	0.39
5	8	20	40	45	65.17	65.38	−0.2117
6	10	20	40	45	66.34	66.37	−0.0317
7	10	20	30	45	69.47	69.7	−0.2333
8	7	22	35	60	85.13	83.9	1.23
9	9	22	45	60	83.46	82.45	1.01
10	9	22	35	60	93.46	93.46	0
11	10	20	40	75	79.41	79.89	−0.4767
12	9	26	35	60	87.56	87.95	−0.39
13	8	24	40	75	80	79.93	0.0733
14	9	22	35	60	93.46	93.46	0
15	10	20	30	75	86.31	84.72	1.59
16	9	22	35	60	93.46	93.46	0
17	10	24	30	75	88	87.95	0.0517
18	10	24	40	75	82	81.93	0.0733
19	9	22	35	60	93.46	93.46	0
20	8	20	30	45	68.12	68.03	0.0867
21	9	22	35	60	93.46	93.46	0
22	10	24	30	45	75.86	75.02	0.8417
23	11	22	35	60	86.33	87.56	−1.23
24	8	20	40	75	78.53	79.21	−0.6817
25	10	24	40	45	71.16	70.5	0.6583
26	8	24	30	45	72.34	72.02	0.3167
27	9	22	35	60	93.46	93.46	0
28	8	24	30	75	85.46	85.27	0.1917
29	9	22	25	60	90.11	91.12	−1.01
30	9	22	35	60	93.46	93.46	0

Table 1. The effect of input parameters used in the modelling with actual and predicted values for CR dye degradation (%).

CR by the desirability factor of 1.00. The optimum value of the independent factor and the desirability value is illustrated in Fig. 8. The actual degradation efficiency of CR was observed to be 93.46% according to run number 16, which is fairly consistent with the value predicted (93.51%). Meanwhile, pure $NiCo_2S_4$ nanoparticles showed 60.23% degradation under similar conditions. The results show the RSM model's significance for optimizing the reaction conditions for CR degradation.

The photodegradation experiment of CR dye was carried out at pH of 9, initial dye concentration of 35 ppm and catalyst dosage of 22 mg, and the degradation kinetics was plotted. Figure 9 shows the profile of the photodegradation of CR and the kinetics. The degradation of CR followed a pseudo-first-order model with a rate constant of 0.043 min^{-1}. The synthesized $NiCo_2S_4$/Ch has a higher photodegradation rate than pure $NiCo_2S_4$ nanoparticles. The photocatalytic degradation of CR proceeds via the formation of aromatic intermediate products detected by the HRLCMS, as shown in Fig. 10. The attack of electrons, hydroxyl radicals and the addition of protons formed the intermediates. A plausible mechanism of the photocatalytic degradation pathway of CR dye based on the LCMS analysis is shown in Fig. 10b.

Scavenging tests

The concentration of ROS attacking the target molecules considerably impacts the rate of degradation processes[62]. To examine the role of the photogenerated electrons, holes, $OH^{\cdot}$ and $O_2^{-\cdot}$ radicals on the photodegradation of CR, some sacrificial reagents were added before irradiating the reaction mixture to trap these species and to know which one of them was responsible for the most CR degradation[11]. Sodium carbonate (Na_2CO_3) as an $OH^{\cdot}$ scavenger, benzoquinone (BQ) as an $O_2^{-\cdot}$ scavenger, potassium persulfate ($K_2S_2O_8$) as an e^- scavenger and disodium EDTA (Na_2EDTA) as an h^+ scavenger were used. As seen in Fig. 11a, BQ and Na_2CO_3 significantly retarded the degradation of CR, signifying that $O_2^{-\cdot}$ and $OH^{\cdot}$ played a major role in the degradation of CR dye by $NiCo_2S_4$/Ch nanocomposite. Similar results were also reported in the literature[64].

Source	Sum of squares	Degree of freedom (Df)	Mean square	F-value	*P*-value	
Model	2600.5	14	185.75	219.11	< 0.0001	Significant
A-pH	20.2	1	20.2	23.83	0.0002	
B-Catalyst dosage	54.54	1	54.54	64.34	< 0.0001	
C-Dye conc	112.84	1	112.84	133.11	< 0.0001	
D-Time	716.1	1	716.1	844.72	< 0.0001	
AB	1.76	1	1.76	2.07	0.1707	
AC	0.4624	1	0.4624	0.5455	0.4716	
AD	0.0992	1	0.0992	0.117	0.737	
BC	1.4	1	1.4	1.66	0.2176	
BD	4.37	1	4.37	5.15	0.0384	
CD	2.27	1	2.27	2.67	0.1229	
A^2	95.6	1	95.6	112.78	< 0.0001	
B^2	116.28	1	116.28	137.17	< 0.0001	
C^2	71.29	1	71.29	84.09	< 0.0001	
D^2	825.13	1	825.13	973.34	< 0.0001	
Residual	12.72	15	0.8477			
Lack of Fit	12.72	8	1.59			
Pure error	0	7	0			
Cor total	2613.22	29				
Quadratic summary statics response	**R^2**	**Adj R^2**	**Pred R^2**	**Std. Dev**	**CV %**	**Adq precision**
	0.995	0.990	0.961	0.920	1.11	43.127

Table 2. Results of analysis of variance of the degradation of CR by $NiCo_2S_4$/Ch nanocomposite.

Performance and reusability studies

The photocatalytic performance of $NiCo_2S_4$/Ch nanocomposite for the degradation of other dyes has also been investigated. The photocatalytic degradation of congo red (CR), methylene blue (MB), methyl orange (MO), rhodamine B (RhB), crystal violet (CV) and rose Bengal (RB) were also investigated. As seen in Fig. 11b, the prepared photocatalyst showed excellent photocatalytic activity towards the degradation of these dyes with efficiency greater than 80%, suggesting great potential for the removal of dyes from the aqueous phase.

The recyclability and stability of the synthesized $NiCo_2S_4$/Ch nanocomposite were investigated, and the results are shown in Fig. 11c. The catalyst was centrifuged, washed with an ethanol solution, and dried in the oven at 60 °C for 2 h before being utilized for another cycle. The $NiCo_2S_4$/Ch nanocomposite could be reused and recycled for four successive cycles and showed an efficiency of 79.62 ± 1.23% after the fourth run. A minor decrease in the photocatalytic efficiency was attributed to the blockage of active sites by the degradation products of the CR dye and disruption in the pore structure of the photocatalyst during recycling. The XRD and SEM images of the reused photocatalyst are shown in Fig. 11d,e. The photocatalyst showed no significant change in the phase and morphology. All the peaks corresponding to $NiCo_2S_4$ were visible in the XRD spectrum of the reused photocatalyst. It is worth mentioning that the intensity of the peak of chitosan at 20° was decreased, possibly due to the accumulation of degradation products over the surface of the photocatalyst. However, the SEM image showed the $NiCo_2S_4$ nanoparticles were dispersed over a chitosan sheet, indicating the prepared photocatalyst maintained its structure after four cycles. Additionally, the absorbance spectra of reused $NiCo_2S_4$/Ch photocatalyst (Fig. 11f) showed a slight increase in the intensity in the UV region, which could be due to the adsorption of degradation intermediate products over the surface of the photocatalyst. The high stability and recyclability of the $NiCo_2S_4$/Ch photocatalyst was attributed to the support of the chitosan matrix.

Mechanism of photodegradation of CR by $NiCo_2S_4$/Ch

The valence and conduction band edge potential of $NiCo_2S_4$ plays a critical role in understanding the photocatalytic degradation mechanism of CR dye. The band positions of $NiCo_2S_4$ were calculated using Mullikan theory[65]. The bandgap and the absolute electronegativity of $NiCo_2S_4$ were calculated to be 2.2 eV[66]. The calculated valance band and conduction band positions of $NiCo_2S_4$ are + 1.93 eV and − 0.27 eV, respectively. A schematic illustration of the photodegradation mechanism of CR dye is shown in Fig. 12. When $NiCo_2S_4$/Ch was irradiated under visible light, the e^- are excited from the valance band (VB) to the conduction band (CB) of $NiCo_2S_4$. The excitation of electrons leaves a positive vacancy (h^+) in the VB. The electron-rich functional groups delocalize the photogenerated holes over the chitosan surface[67]. The photogenerated electrons are absorbed by the oxygen molecules, generating $O_2^{\cdot-}$ radicals. Meanwhile, the water molecules absorb the holes, producing $OH^{\cdot}$ radicals. These radicals initiate a series of photocatalytic reactions attacking the CR molecules and bringing their degradation into simpler molecules[68]. The surface of chitosan and the functional groups helps to retain CR dye molecules over the photocatalyst's surface, while the ROS generated by $NiCo_2S_4$ degrade it. The hydroxyl groups of chitosan strongly attract the positively charged nitrogen of the CR dye[69]. Moreover, chitosan helps in

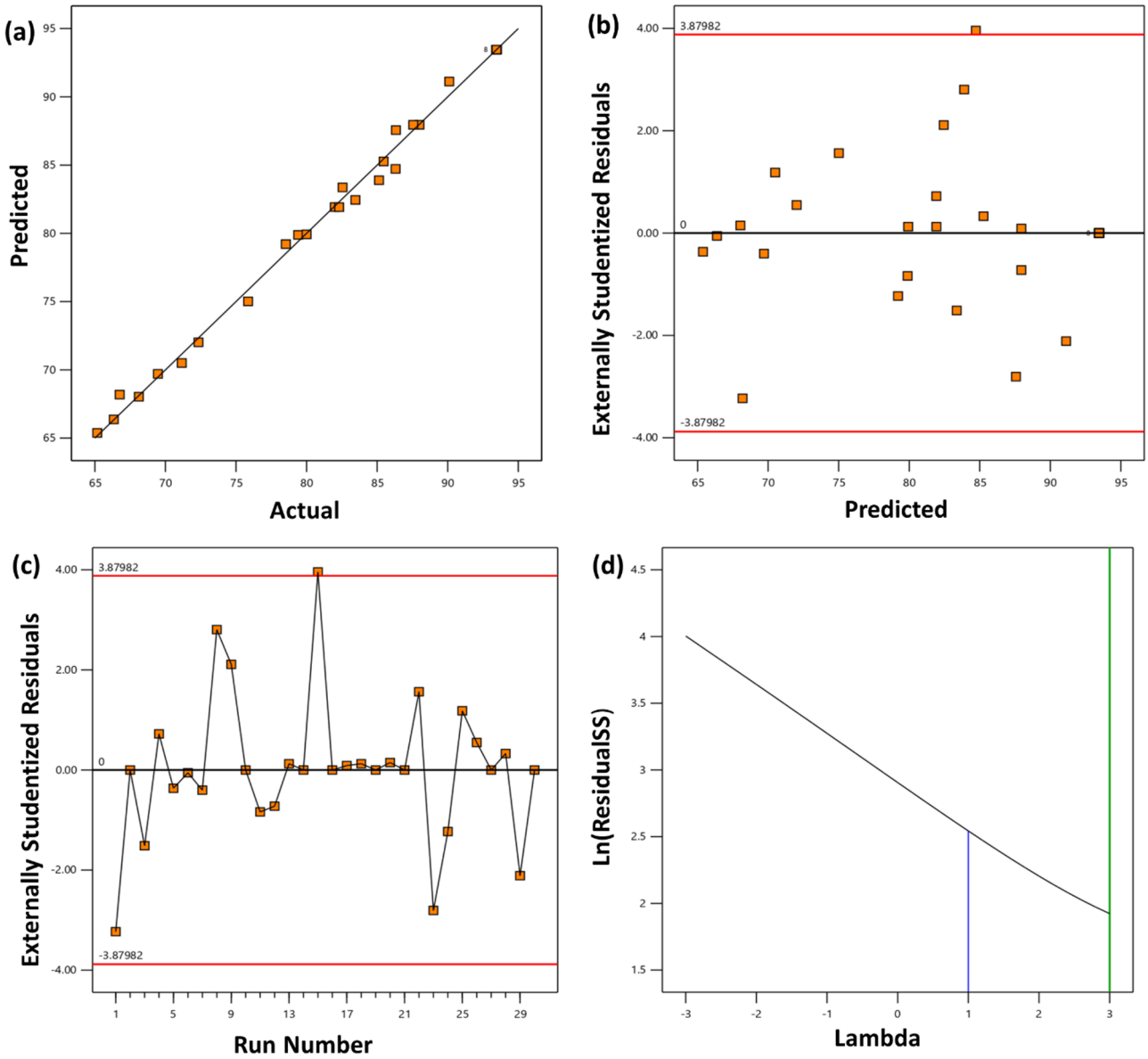

Figure 6. (**a**) Predicted vs actual diagram, (**b**) residuals vs predicted diagram, (**c**) residuals vs run number and (**d**) Box-cox plot for the power transformations for the degradation of CR.

charge of delocalization and enhances photocatalytic efficiency[70]. The photocatalytic reactions responsible for the degradation of CR are as follows[71]:

$$NiCo_2S_4/Ch \xrightarrow{h\nu} NiCo_2S_4/Ch(e^- + h^+) \tag{7}$$

$$e^- + O_2 \rightarrow O_2^{-\bullet} \tag{8}$$

$$h^+ + OH^- \rightarrow OH^{\bullet} \tag{9}$$

$$h^+ + H_2O \rightarrow H_2O_2 + H^+ \tag{10}$$

$$H_2O_2 + e^- \rightarrow OH^- \tag{11}$$

$$H_2O_2 \xrightarrow{h\nu} 2OH^{\bullet} \tag{12}$$

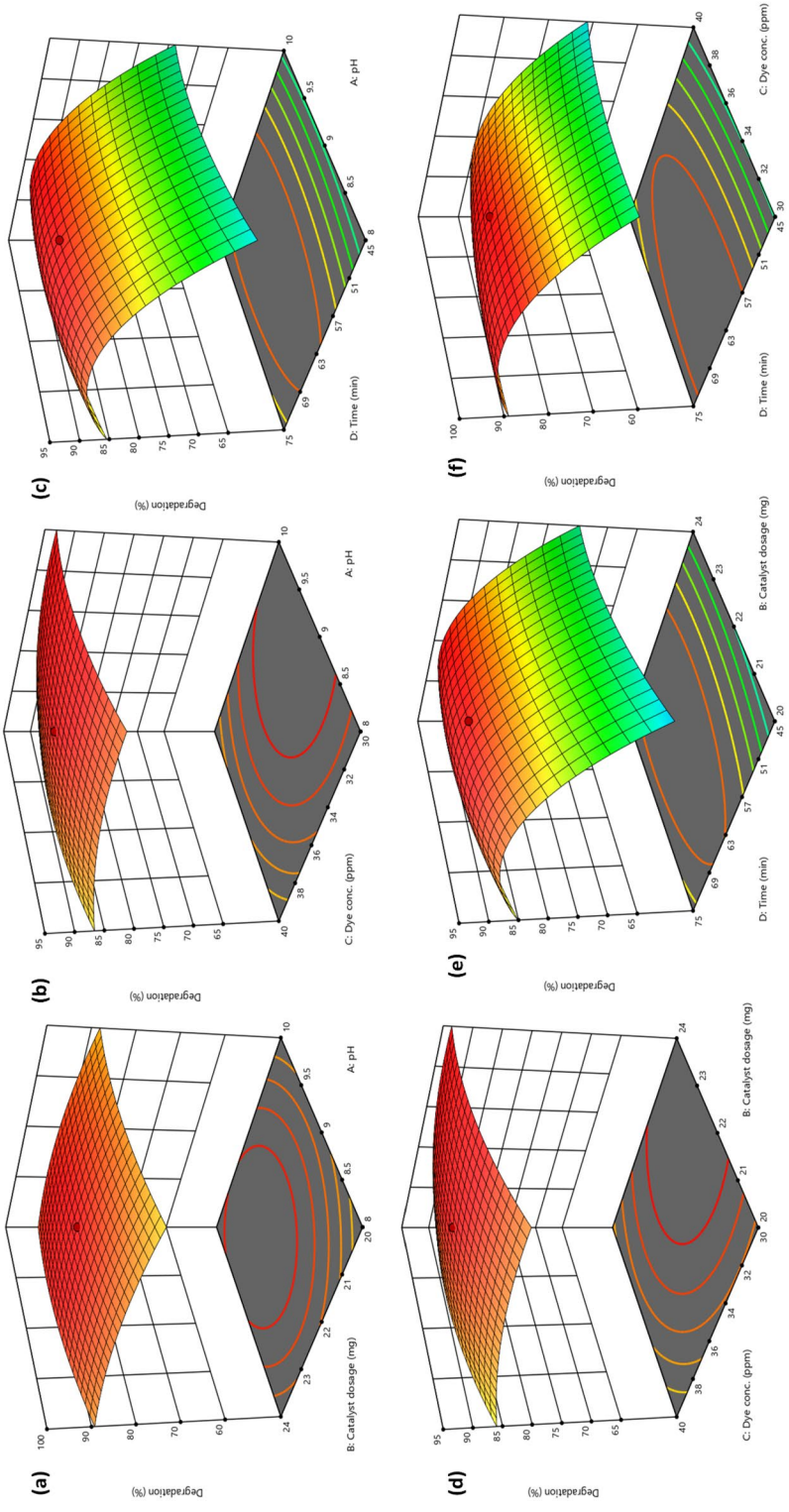

Figure 7. 3D surface graphs for the relation between (**a**) pH and catalyst dosage, (**b**) pH and dye concentration, (**c**) pH and time, (**d**) catalyst dosage and dye concentration, (**e**) catalyst dosage and time and (**f**) dye concentration and time.

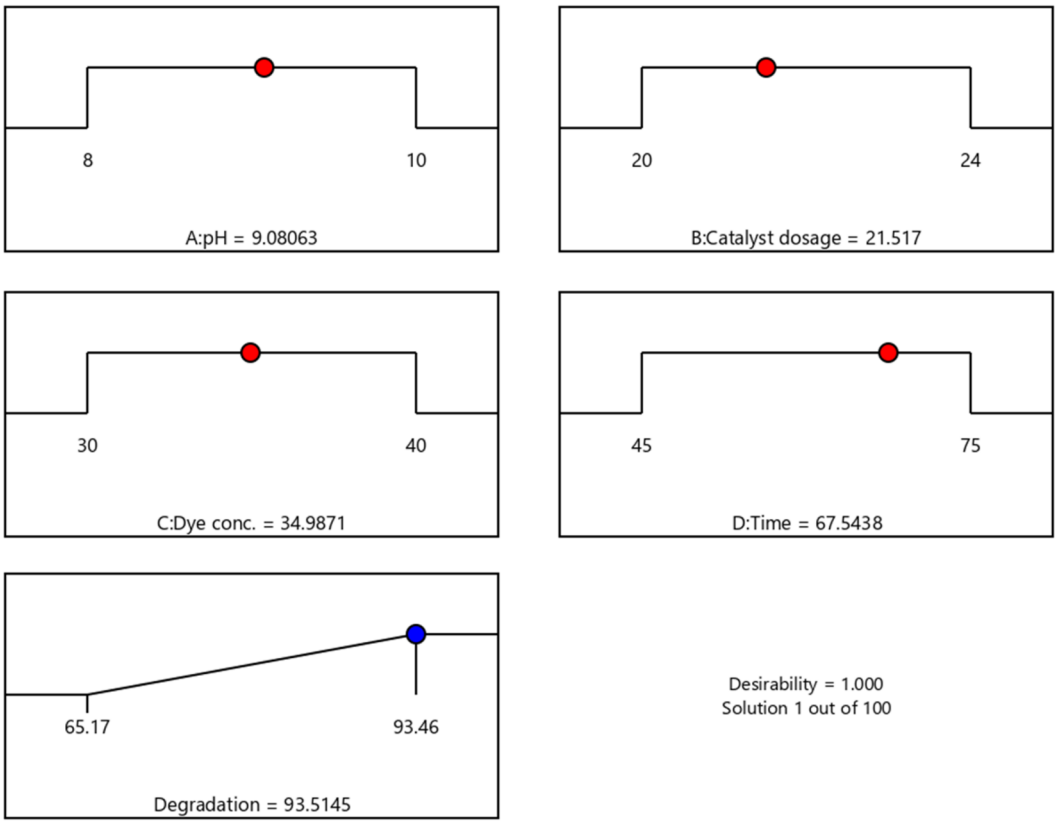

Figure 8. The desirability under optimum conditions.

$$CR + OH^{\bullet} + O_2^{-\bullet} \rightarrow Degradation\ products \tag{13}$$

Comparison with other reported photocatalysts
Various materials have been reported to remove CR from the aqueous phase. As prepared, $NiCo_2S_4$/Ch nanocomposite outperformed most of the reported photocatalysts to degrade CR, as shown in Table 3.

Conclusion

The present study was consistent in assessing the photocatalytic performance of the fabricated $NiCo_2S_4$/Ch nanocomposite and the impacts of different reaction parameters on the photodegradation of CR dye. The effect of pH, photocatalyst dosage, initial dye concentration and irradiation time on the photodegradation of congo red was examined using RSM employing a CCD. According to the ANOVA analysis, a maximum degradation of 93.51% could be attained at the optimum pH of 9, photocatalyst dosage of 22 mg, and CR concentration of 35 ppm in 60 min with a desirability value of 1. Additionally, the statistical parameters like Adj R^2, Pred R^2, CV % and Adq precision justified the adequacy of the suggested quadratic model. The synthesized $NiCo_2S_4$/Ch nanocomposite showed a photodegradation efficiency of 93.46% within 60 min under prescribed conditions. The degradation mechanism was studied, and it was found that the composite effectively generated hydroxyl and superoxide radicals that contributed to the photodegradation process. The study emphasizes the possibility of $NiCo_2S_4$/Ch nanocomposite as a recyclable and cost-effective photocatalyst for treating dye-contaminated wastewater.

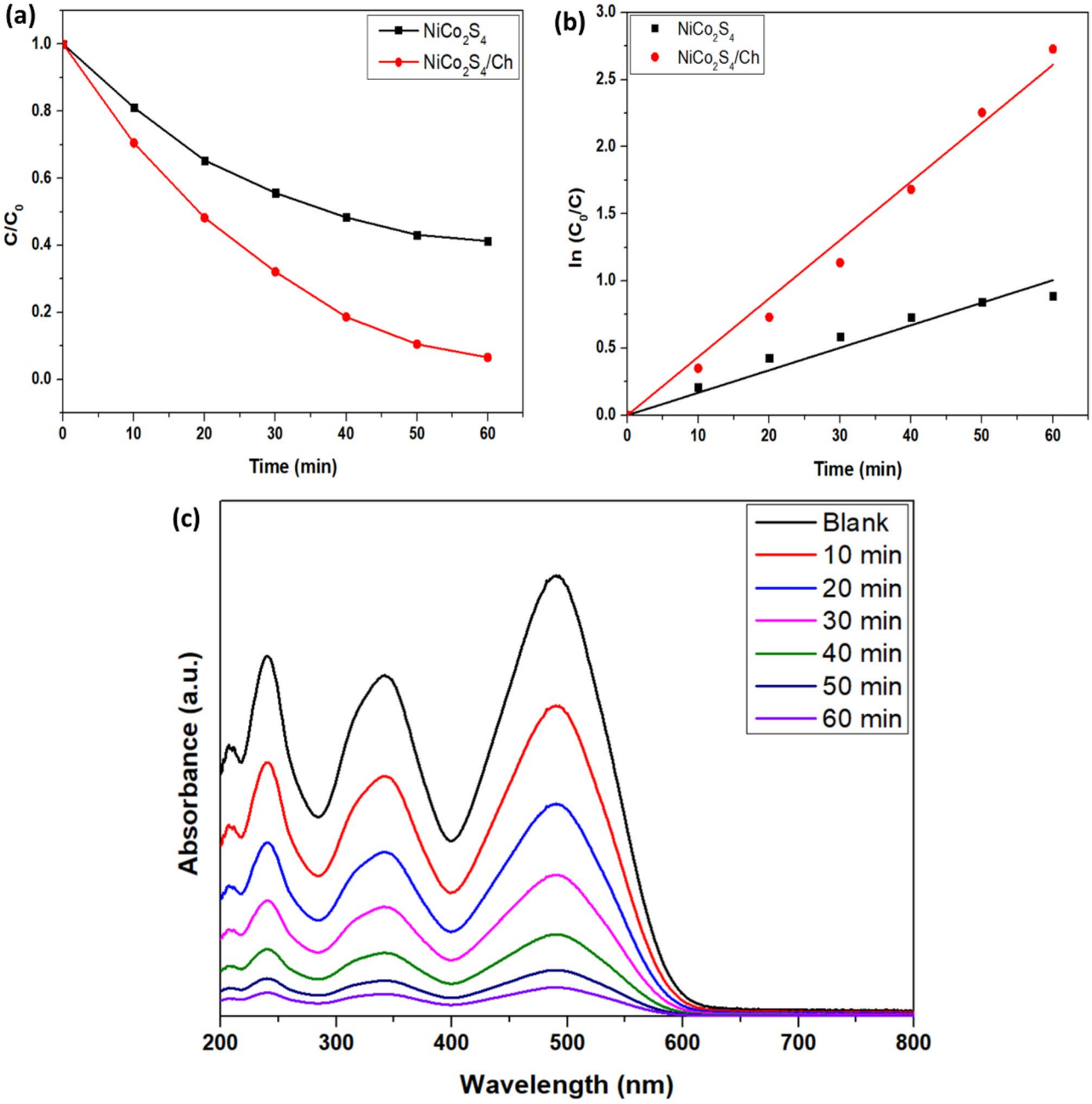

Figure 9. (**a**) Profiles of degradation (**b**) Kinetics and the degradation spectrum of CR dye.

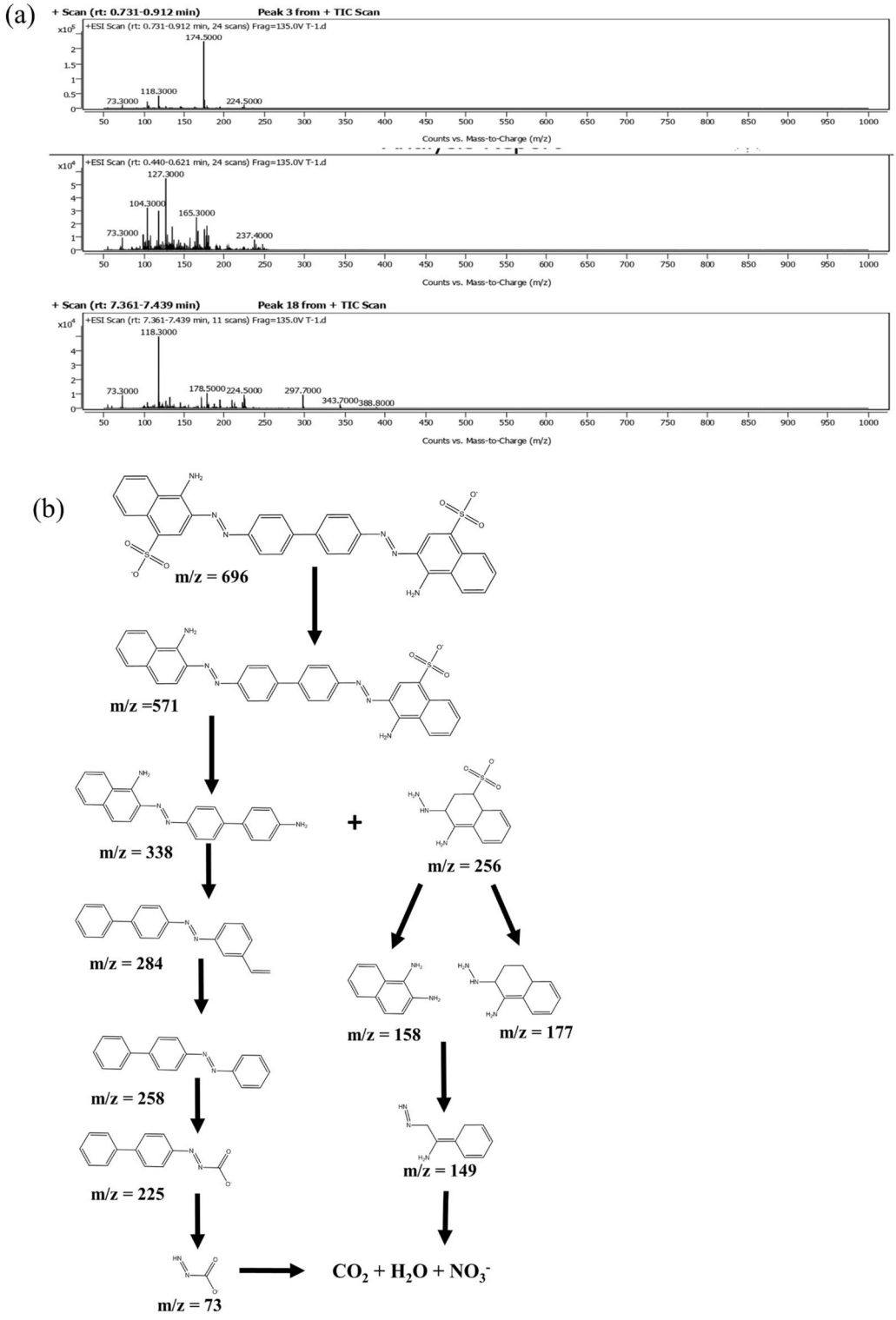

Figure 10. (**a**) Mass spectra of the photodegradation of CR at the intermediate stage and (**b**) plausible mechanism of the degradation of CR dye.

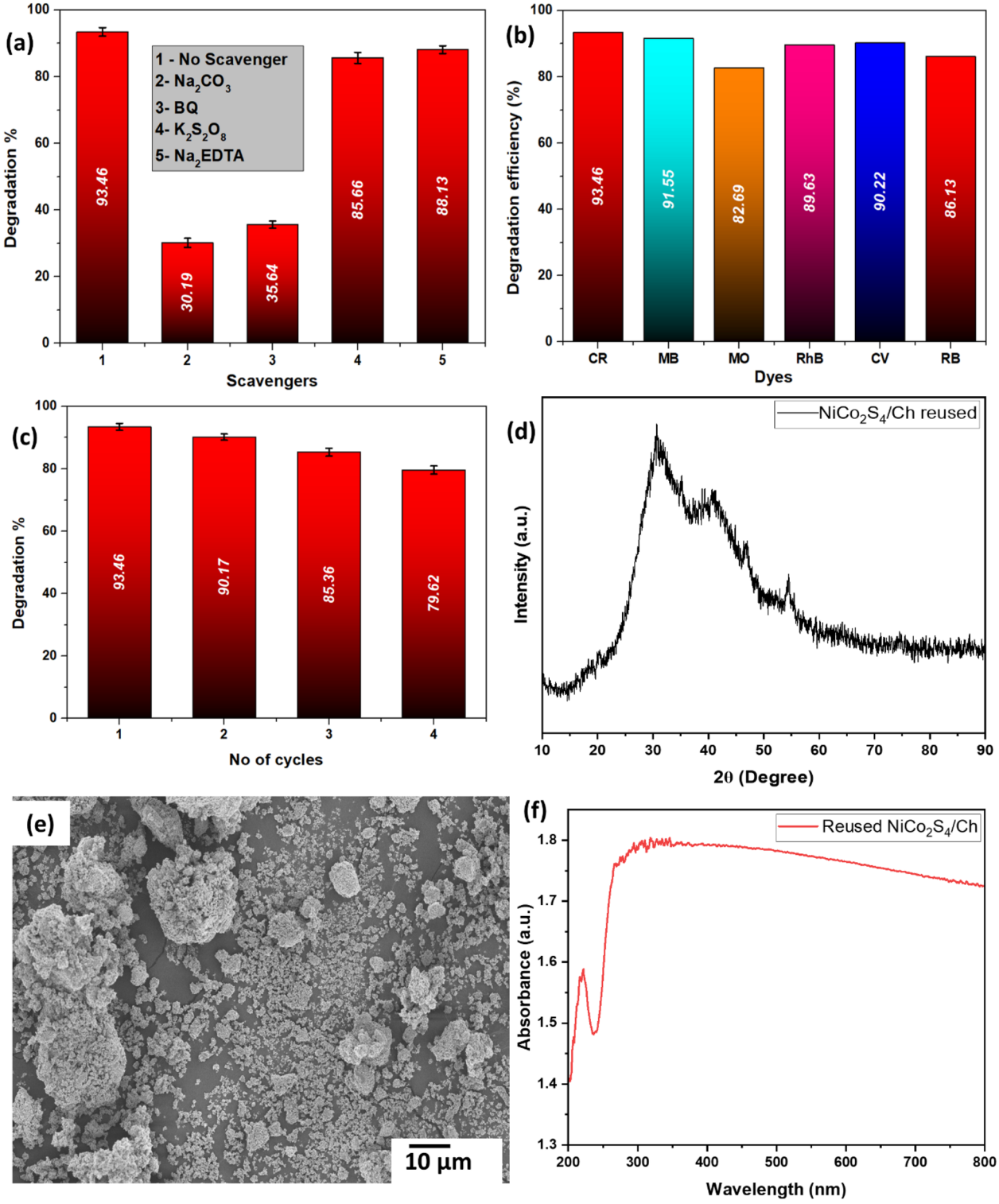

Figure 11. (**a**) Effect of scavenging agents, (**b**) degradation percentage of other dyes, (**c**) reusability performance of $NiCo_2S_4$/Ch, (**d**) XRD spectrum, (**e**) SEM image and (**f**) absorbance spectrum of reused $NiCo_2S_4$/Ch.

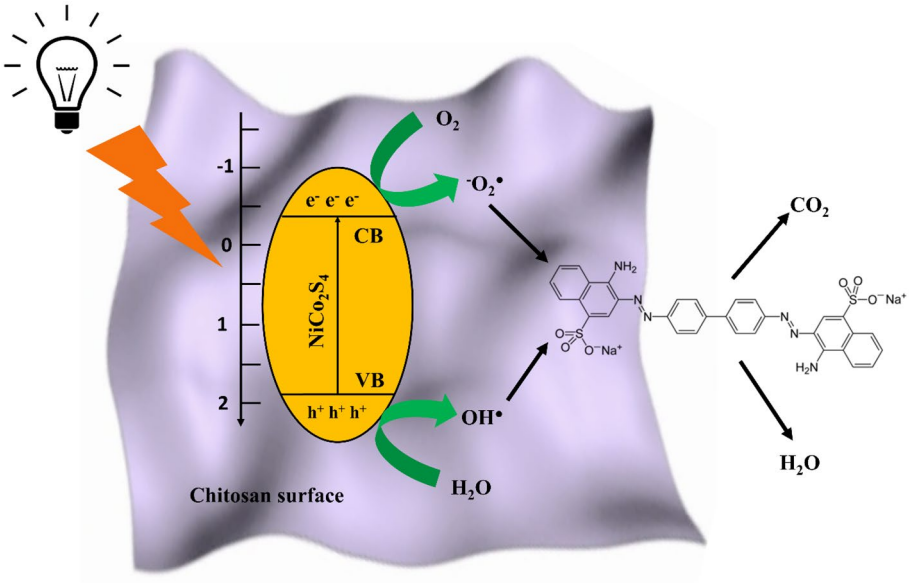

Figure 12. Mechanism of photocatalytic degradation of CR.

Photocatalyst	Intial CR concentration (ppm)	Photocatalyst dosage (g/L)	Irradiation source	Time (min)	Degradation (%)	References
Ag_2WO_4/Ag_2S	20	1	200 W Xe lamp	140	99.5	[72]
f–FeO–NC	20	0.2	Sunlight	120	99	[73]
$PbTiO_3$	1×10^{-5} M	0.5	150 W Xe lamp	150	92	[74]
SrPO NPs	20	1	200 W Xe lamp	210	67	[75]
ZnO	20	0.5	100 W Xe lamp	120	85	[76]
$NiCo_2S_4$/Ch	35	0.44	23 W Philips LED	60	93.46	Present work

Table 3. Comparison of $NiCo_2S_4$/Ch with other reported materials for the photodegradation of CR dye.

Data availability

All data generated or analyzed during this study are included in this published article.

Received: 11 October 2023; Accepted: 8 January 2024
Published online: 11 January 2024

References

1. Gadore, V. & Ahmaruzzaman, M. Tailored fly ash materials: A recent progress of their properties and applications for remediation of organic and inorganic contaminants from water. *J. Water Process Eng.* **41**, 101910 (2021).
2. Mishra, S. R. & Ahmaruzzaman, M. Tin oxide based nanostructured materials: Synthesis and potential applications. *Nanoscale* **14**, 1566–1605 (2022).
3. Issa, M. A. & Abidin, Z. Z. Sustainable development of enhanced luminescence polymer-carbon dots composite film for rapid Cd2+ removal from wastewater. *Molecules* **25**, 3541 (2020).
4. Mishra, S. R. & Ahmaruzzaman, M. Microplastics: Identification, toxicity and their remediation from aqueous streams. *Sep. Purif. Rev.* https://doi.org/10.1080/15422119.2022.2096071 (2022).
5. Jabbar, Z. H. & Esmail Ebrahim, S. Recent advances in nano-semiconductors photocatalysis for degrading organic contaminants and microbial disinfection in wastewater: A comprehensive review. *Environ. Nanotechnol. Monit. Manag.* **17**, 100666 (2022).
6. Issa, M. A. *et al.* Facile synthesis of nitrogen-doped carbon dots from lignocellulosic waste. *Nanomaterials* **9**, 1500 (2019).
7. Jabbar, Z. H., Graimed, B. H., Okab, A. A., Alsunbuli, M. M. & Al-husseiny, R. A. Construction of 3D flower-like $Bi_5O_7I/Bi/Bi_2WO_6$ heterostructure decorated $NiFe_2O_4$ nanoparticles for photocatalytic destruction of Levofloxacin in aqueous solution: Synergistic effect between S-scheme and SPR action. *J. Photochem. Photobiol. A Chem.* **441**, 114734 (2023).
8. Mishra, S. R. & Ahmaruzzaman, M. CuO and CuO-based nanocomposites: Synthesis and applications in environment and energy. *Sustain. Mater. Technol.* **33**, e00463 (2022).
9. Gadore, V., Mishra, S. R. & Ahmaruzzaman, M. Bio-inspired sustainable synthesis of novel SnS_2/biochar nanocomposite for adsorption coupled photodegradation of amoxicillin and congo red: Effects of reaction parameters, and water matrices. *J. Environ. Manag.* **334**, 117496 (2023).
10. Bhuyan, A. & Ahmaruzzaman, M. Metal-organic frameworks: A new generation potential material for aqueous environmental remediation. *Inorg. Chem. Commun.* **140**, 109436 (2022).
11. Gadore, V., Mishra, S. R. & Ahmaruzzaman, M. Facile green synthesis of SnS2 nanoparticles using Tulsi extract: insight into the optical and photocatalytic properties. *Int. J. Environ. Anal. Chem.* 1–18 (2023).

12. Jabbar, Z. H., Ammar, S. H. & Esmail Ebrahim, S. Enhanced visible-light photocatalytic bacterial inhibition using recyclable magnetic heterogeneous nanocomposites (Fe_3O_4@SiO_2@Ag_2WO_4@Ag_2S) in core/shell structure. *Environ. Nanotechnol. Monit. Manag.* **16**, 100601 (2021).
13. Gadore, V. & Ahmaruzzaman, M. M. Fly ash–based nanocomposites: A potential material for effective photocatalytic degradation/elimination of emerging organic pollutants from aqueous stream. *Environ. Sci. Pollut. Res.* **28**, 46910–46933 (2021).
14. Gadore, V., Mishra, S. R. & Ahmaruzzaman, M. Bandgap engineering approach for synthesising photoactive novel Ag/HAp/SnS_2 for removing toxic anti-fungal pharmaceutical from aqueous environment. *J. Hazard. Mater.* https://doi.org/10.1016/J.JHAZMAT.2023.132458 (2023).
15. Mishra, S. R., Gadore, V. & Ahmaruzzaman, M. Inorganic–organic hybrid quantum dots for AOP-mediated photodegradation of ofloxacin and para-nitrophenol in diverse water matrices. *NPJ Clean Water* **6**, 1–24 (2023).
16. Ranjan Mishra, S., Gadore, V. & Ahmaruzzaman, M. Novel 3D sphere-like β-In2S3/Biochar nanoflowers for remediation of dyes in single and binary systems and interpretation using statistical physical modeling. *Environ. Nanotechnol. Monit. Manag.* **20**, 100807 (2023).
17. Sunaina, *et al.* Surface photosensitization of ZnO by ZnS to enhance the photodegradation efficiency for organic pollutants. *SN Appl. Sci.* **3**, 689 (2021).
18. Song, Z. *et al.* Magnetic grinding synthesis of copper sulfide-based photocatalytic composites for the degradation of organic dyes under visible light. *New J. Chem.* **47**, 2286–2295 (2023).
19. Zhang, L. *et al.* Effective charge separation and enhanced photocatalytic activity by the heterointerface in MoS_2/reduced graphene oxide composites. *RSC Adv.* **6**, 60318–60326 (2016).
20. Ahmaruzzaman, M. & Gadore, V. MoS2 based nanocomposites: An excellent material for energy and environmental applications. *J. Environ. Chem. Eng.* **9**, 105836 (2021).
21. Thambidurai, M. *et al.* Studies on optical absorption and structural properties of Fe doped CdS quantum dots. *Solid State Sci.* **12**, 1554–1559 (2010).
22. Lu, F. *et al.* Engineering sulfur vacancies and impurities in $NiCo_2S_4$ nanostructures toward optimal supercapacitive performance. *Nano Energy* **26**, 313–323 (2016).
23. Shen, J. *et al.* Controlled synthesis and comparison of $NiCo_2S_4$/graphene/2D TMD ternary nanocomposites for high-performance supercapacitors. *Chem. Commun.* **52**, 9251–9254 (2016).
24. Xia, C., Li, P., Gandi, A. N., Schwingenschlögl, U. & Alshareef, H. N. Is $NiCo_2S_4$ really a semiconductor?. *Chem. Mater.* **27**, 6482–6485 (2015).
25. Li, W. *et al.* In situ electronic redistribution tuning of $ZnIn_2S_4$ nanosheets on $NiCo_2S_4$ hollow tube for boosted photocatalytic hydrogen evolution. *Appl. Surf. Sci.* **598**, 153801 (2022).
26. Wang, Z., Nengzi, L. C., Zhang, X., Zhao, Z. & Cheng, X. Novel $NiCo_2S_4$/CS membranes as efficient catalysts for activating persulfate and its high activity for degradation of nimesulide. *Chem. Eng. J.* **381**, 122517 (2020).
27. Pandey, N., Shukla, S. K. & Singh, N. B. Water purification by polymer nanocomposites: An overview. *Nanocomposites* **3**, 47–66. https://doi.org/10.1080/20550324.2017.1329983 (2017).
28. Sirajudheen, P. & Meenakshi, S. Facile synthesis of chitosan-La3+-graphite composite and its influence in photocatalytic degradation of methylene blue. *Int. J. Biol. Macromol.* **133**, 253–261 (2019).
29. Khan, A., Badshah, S. & Airoldi, C. Biosorption of some toxic metal ions by chitosan modified with glycidylmethacrylate and diethylenetriamine. *Chem. Eng. J.* **171**, 159–166 (2011).
30. Bandara, S., Du, H., Carson, L., Bradford, D. & Kommalapati, R. Agricultural and biomedical applications of chitosan-based nanomaterials. *Nanomater* **10**, 1903 (2020).
31. Thakur, V. K. & Voicu, S. I. Recent advances in cellulose and chitosan based membranes for water purification: A concise review. *Carbohydr. Polym.* **146**, 148–165 (2016).
32. Hamad, H., Bassyouni, D., El-Ashtoukhy, E. S., Amin, N. & Abd El-Latif, M. Electrocatalytic degradation and minimization of specific energy consumption of synthetic azo dye from wastewater by anodic oxidation process with an emphasis on enhancing economic efficiency and reaction mechanism. *Ecotoxicol. Environ. Saf.* **148**, 501–512 (2018).
33. Mishra, S. R., Gadore, V., Ghotekar, S. & Ahmaruzzaman, M. Insights into the enhanced photocatalytic and antioxidant properties of novel biogenically synthesised β-In2S3 quantum dots. *Int. J. Environ. Anal. Chem.* https://doi.org/10.1080/03067319.2023.2186228 (2023).
34. Hasanpour, M., Motahari, S., Jing, D. & Hatami, M. Statistical analysis and optimization of photodegradation efficiency of methyl orange from aqueous solution using cellulose/zinc oxide hybrid aerogel by response surface methodology (RSM). *Arab. J. Chem.* **14**, 103401 (2021).
35. Sakkas, V. A., Islam, M. A., Stalikas, C. & Albanis, T. A. Photocatalytic degradation using design of experiments: A review and example of the Congo red degradation. *J. Hazard. Mater.* **175**, 33–44 (2010).
36. Bose, S., Tripathy, B. K., Debnath, A. & Kumar, M. Boosted sono-oxidative catalytic degradation of brilliant green dye by magnetic $MgFe_2O_4$ catalyst: Degradation mechanism, assessment of bio-toxicity and cost analysis. *Ultrason. Sonochem.* **75**, 105592 (2021).
37. Jiang, J. *et al.* A PEGylated deep eutectic solvent for controllable solvothermal synthesis of porous $NiCo_2S_4$ for efficient oxygen evolution reaction. *Green Chem.* **19**, 3023–3031 (2017).
38. Rhim, J. W., Hong, S. I., Park, H. M. & Ng, P. K. W. Preparation and characterization of chitosan-based nanocomposite films with antimicrobial activity. *J. Agric. Food Chem.* **54**, 5814–5822 (2006).
39. Rajesh Kumar, B. & Hymavathi, B. X-ray peak profile analysis of solid-state sintered alumina doped zinc oxide ceramics by Williamson-Hall and size-strain plot methods. *J. Asian Ceram. Soc.* **5**, 94–103 (2017).
40. Mahmoud, Z. H., Hamrouni, A., Kareem, A. B., Mostafa, M. A. & Majeed, A. H. Synthesis and characterization of chitosan sheet modified by varied weight ratio of anatase (TiO2) nano mixture with Cr (VI) adsorbing. *Kuwait J. Sci.* (2023).
41. Sirajudheen, P., Resha Kasim, V. C., Nabeena, C. P., Basheer, M. C. & Meenakshi, S. Tunable photocatalytic oxidation response of ZnS tethered chitosan-polyaniline composite for the removal of organic pollutants: A mechanistic perspective. *Mater. Today Proc.* **47**, 2553–2559 (2021).
42. Vieira, R. S., Oliveira, M. L. M., Guibal, E., Rodríguez-Castellón, E. & Beppu, M. M. Copper, mercury and chromium adsorption on natural and crosslinked chitosan films: An XPS investigation of mechanism. *Colloids Surf. A Physicochem. Eng. Asp.* **374**, 108–114 (2011).
43. Yang, X. *et al.* Perylene-functionalized graphene sheets modified with chitosan for voltammetric discrimination of tryptophan enantiomers. *Microchim. Acta* **186**, 1–12 (2019).
44. Mishra, S. R., Roy, P., Gadore, V. & Ahmaruzzaman, M. A combined experimental and modeling approach to elucidate the adsorption mechanism for sustainable water treatment via In2S3-anchored chitosan. *Sci. Rep.* **13**, 1–24 (2023).
45. Briggs, D. Handbook of X-ray photoelectron spectroscopy. In Perkin-Elmer Corp., Physical Electronics Division, Eden Prairie, Minnesota, USA, 1979 (eds. Wanger, C. D. Riggs, W. M., Davis, L. E., Moulder J. F. & Muilenberg G. E.), 190 pp. $195. *Surf. Interface Anal.* **3**, v–v (1981).
46. Gieroba, B. *et al.* Spectroscopic studies on the temperature-dependent molecular arrangements in hybrid chitosan/1,3-β-D-glucan polymeric matrices. *Int. J. Biol. Macromol.* **159**, 911–921 (2020).
47. Jiang, K. *et al.* Noble metal-free $NiCo_2S_4$/CN sheet-on-sheet heterostructure for highly efficient visible-light-driven photocatalytic hydrogen evolution. *J. Alloys Compd.* **853**, 157284 (2021).

48. Li, C. *et al.* $NiCo_2S_4$ decorated gC3N4 nanosheets for enhanced photocatalytic hydrogen evolution. *J. Nanoparticle Res.* **22**, 1–12 (2020).
49. Mishra, S. R. *et al.* In_2S_3 incorporated into CO_3^{2-}@Ni/Fe/Zn trimetallic LDH as a bi-functional novel nanomaterial for enzymatic urea sensing and removal of sulfur-containing pharmaceutical from aqueous streams. *Chem. Eng. J.* https://doi.org/10.1016/J.CEJ.2023.146207 (2023).
50. Mishra, S. R., Gadore, V. & Ahmaruzzaman, M. Insights into persulfate-activated photodegradation of tinidazole and photoreduction of hexavalent chromium through β-In_2S_3 anchored on Ag-doped fish scale-derived HAp composite quantum dots. *J. Clean. Prod.* **427**, 139221 (2023).
51. Melo-Silveira, R. F. *et al.* In vitro antioxidant, anticoagulant and antimicrobial activity and in inhibition of cancer cell proliferation by Xylan extracted from corn cobs. *Int. J. Mol. Sci.* **13**, 409–426 (2011).
52. Taha, A. *et al.* Green synthesis of an activated carbon-supported Ag and ZnO nanocomposite for photocatalytic degradation and its antibacterial activities. *Molecules* **25**, 1586 (2020).
53. Pandian, S. R. K., Deepak, V., Kalishwaralal, K. & Gurunathan, S. Biologically synthesized fluorescent CdS NPs encapsulated by PHB. *Enzym. Microb. Technol.* **48**, 319–325 (2011).
54. Zhu, Y. *et al.* Mesoporous $NiCo_2S_4$ nanoparticles as high-performance electrode materials for supercapacitors. *J. Power Sources* **273**, 584–590 (2015).
55. Gadore, V., Mishra, S. R. & Ahmaruzzaman, M. Green and environmentally sustainable fabrication of SnS_2 quantum dots/chitosan nanocomposite for enhanced photocatalytic performance: Effect of process variables, and water matrices. *J. Hazard. Mater.* **444**, 130301 (2023).
56. Gadore, V., Ranjan Mishra, S. & Ahmaruzzaman, M. SnS_2 modified carbonate-intercalated Ni–Zn–Fe trimetallic LDH as a novel photocatalyst for persulfate activation: Influence of operational parameters, co-existing ions and organic compounds. *Chem. Eng. J.* **475**, 146157 (2023).
57. Yadav, G. *et al.* Biogenic growth of egg shell–derived $CaMn_2O_4$ over tailored FLY ASH surface for synergistically photodegradation of ofloxacin: materialistic and chemical studies. *Biomass Convers. Biorefinery* 1–18 (2023).
58. Idrees, S. A. & Ibrahim, M. K. Optimization of congo-red photo-catalytic degradation by central composite design. In *2018 International Conference on Advanced Science and Engineering (ICOASE)* 389–393 (IEEE, 2018).
59. Tripathi, P., Tiwari, S., Sonwani, R. K. & Singh, R. S. A step towards enhancing the efficiency of biofilm mediated degradation of brilliant green dye in packed bed bioreactor: Statistical and toxicity analysis. *Process Saf. Environ. Prot.* **170**, 1228–1239 (2023).
60. Hosseini-Nasab, S. J., Saber-Tehrani, M., Haghgoo, M. & Aberoomand-Azar, P. Control of porous properties of ambient dried sodium silicate-based aerogels using response surface methodology. *J. Thermoplast. Compos. Mater.* 0892705719876316 (2019).
61. Dey, A. K., Mishra, S. R. & Ahmaruzzaman, M. Solar light–based advanced oxidation processes for degradation of methylene blue dye using novel Zn-modified CeO_2@biochar. *Environ. Sci. Pollut. Res.* **30**, 53887–53903 (2023).
62. Gadore, V., Mishra, S. R. & Ahmaruzzaman, M. One-pot synthesis of CdS/CeO_2 heterojunction nanocomposite with tunable bandgap for the enhanced advanced oxidation process. *Sci. Rep.* **13**, 7708 (2023).
63. Mishra, S. R., Gadore, V. & Ahmaruzzaman, M. A critical review on In2S3-based nanomaterial for emerging contaminants elimination through integrated adsorption-degradation technique: Effect of reaction parameters and co-existing species. *J. Hazard. Mater. Lett.* **4**, 100087 (2023).
64. Wang, J., Wang, G., Cheng, B., Yu, J. & Fan, J. Sulfur-doped g-C_3N_4/TiO_2 S-scheme heterojunction photocatalyst for Congo Red photodegradation. *Chin. J. Catal.* **42**, 56–68 (2021).
65. Cao, W., Chen, L. & Qi, Z. Microwave-assisted synthesis of Ag/Ag_2SO_4/ZnO nanostructures for efficient visible-light-driven photocatalysis. *J. Mol. Catal. A Chem.* **401**, 81–89 (2015).
66. Peng, J., Xu, J., Wang, Z., Ding, Z. & Wang, S. Developing an efficient $NiCo_2S_4$ cocatalyst for improving the visible light H_2 evolution performance of CdS nanoparticles. *Phys. Chem. Chem. Phys.* **19**, 25919–25926 (2017).
67. Liang, H., Lv, C., Chen, H., Wu, L. & Hou, X. Facile synthesis of chitosan membranes for visible-light-driven photocatalytic degradation of tetracycline hydrochloride. *RSC Adv.* **10**, 45171–45179 (2020).
68. Yadav, G., Mishra, S. R., Gadore, V., Yadav, N. & Ahmaruzzaman, M. A smart and sustainable pathway for abatement of single and binary mixtures of dyes through magnetically retrievable Ca4Fe9O17 anchored on Biochar matrix. *Sci. Rep.* **131**(13), 1–21 (2023).
69. Chatterjee, S., Lee, M. W. & Woo, S. H. Adsorption of congo red by chitosan hydrogel beads impregnated with carbon nanotubes. *Bioresour. Technol.* **101**, 1800–1806 (2010).
70. Honarmand, M., Naeimi, A., Rezakhani, M. S. & Chaji, M. A. Ni/NiO doped chitosan-cellulose based on the wastes of barley and shrimp for degradation of ciprofloxacin antibiotic. *J. Mater. Res. Technol.* **18**, 4060–4074 (2022).
71. Ahmaruzzaman, M. & Mishra, S. R. Photocatalytic performance of g-C_3N_4 based nanocomposites for effective degradation/removal of dyes from water and wastewater. *Mater. Res. Bull.* **143**, 111417 (2021).
72. Jabbar, Z. H. *et al.* Photocatalytic degradation of Congo red dye using magnetic silica-coated Ag_2WO_4/Ag_2S as Type I heterojunction photocatalyst: Stability and mechanisms studies. *Mater. Sci. Semicond. Process.* **153**, 107151 (2023).
73. Saini, D., Aggarwal, R., Anand, S. R. & Sonkar, S. K. Sunlight induced photodegradation of toxic azo dye by self-doped iron oxide nano-carbon from waste printer ink. *Sol. Energy* **193**, 65–73 (2019).
74. Bhagwat, U. O., Wu, J. J., Asiri, A. M. & Anandan, S. Photocatalytic degradation of congo red using $PbTiO_3$ nanorods synthesized via a sonochemical approach. *ChemistrySelect* **3**, 11851–11858 (2018).
75. Arumugam, B., Muthukutty, B., Chen, S.-M., Amanulla, B. & Ramaraj, S. K. Sustainable one-pot synthesis of strontium phosphate nanoparticles with effective charge carriers for the photocatalytic degradation of carcinogenic naphthylamine derivative. *New J. Chem.* **45**, 15437–15447 (2021).
76. Adam, R. E., Pozina, G., Willander, M. & Nur, O. Synthesis of ZnO nanoparticles by co-precipitation method for solar driven photodegradation of Congo red dye at different pH. *Photonics Nanostruct. Fundam. Appl.* **32**, 11–18 (2018).

Acknowledgements

The authors are thankful to the Director, National Institute of Technology Silchar, for his help and continuous support for the preparation of the manuscript.

Author contributions

V.G. wrote the main manuscript text. A.K.S. modified, revised and edited the manuscript. S.R.M. prepared figures and edited the manuscript and M.A. discussed results, commented, revised and corrected the whole manuscript. All authors reviewed the manuscript.

Competing interests

The authors declare no competing interests.

Additional information

Correspondence and requests for materials should be addressed to M.A.

Reprints and permissions information is available at www.nature.com/reprints.

Publisher's note Springer Nature remains neutral with regard to jurisdictional claims in published maps and institutional affiliations.